Gradients in Wall Mechanics and Polysaccharides along Growing Inflorescence Stems[1][OPEN]

Pyae Phyo,[a,2] Tuo Wang,[a,2,3] Sarah N. Kiemle,[b,2] Hugh O'Neill,[c] Sai Venkatesh Pingali,[c] Mei Hong,[a,4] and Daniel J. Cosgrove[b,4]

[a]Department of Chemistry, Massachusetts Institute of Technology, Cambridge, Massachusetts 02139
[b]Department of Biology, Pennsylvania State University, University Park, Pennsylvania 16802
[c]Biology and Soft Matter Division, Oak Ridge National Laboratory, Oak Ridge, Tennessee 37831

ORCID IDs: 0000-0003-2966-5527 (H.O.); 0000-0001-5255-5858 (M.H.); 0000-0002-4020-5786 (D.J.C.).

At early stages of Arabidopsis (*Arabidopsis thaliana*) flowering, the inflorescence stem undergoes rapid growth, with elongation occurring predominantly in the apical ~4 cm of the stem. We measured the spatial gradients for elongation rate, osmotic pressure, cell wall thickness, and wall mechanical compliances and coupled these macroscopic measurements with molecular-level characterization of the polysaccharide composition, mobility, hydration, and intermolecular interactions of the inflorescence cell wall using solid-state nuclear magnetic resonance spectroscopy and small-angle neutron scattering. Force-extension curves revealed a gradient, from high to low, in the plastic and elastic compliances of cell walls along the elongation zone, but plots of growth rate versus wall compliances were strikingly nonlinear. Neutron-scattering curves showed only subtle changes in wall structure, including a slight increase in cellulose microfibril alignment along the growing stem. In contrast, solid-state nuclear magnetic resonance spectra showed substantial decreases in pectin amount, esterification, branching, hydration, and mobility in an apical-to-basal pattern, while the cellulose content increased modestly. These results suggest that pectin structural changes are connected with increases in pectin-cellulose interaction and reductions in wall compliances along the apical-to-basal gradient in growth rate. These pectin structural changes may lessen the ability of the cell wall to undergo stress relaxation and irreversible expansion (e.g. induced by expansins), thus contributing to the growth kinematics of the growing stem.

When growing at steady state, axial organs such as roots and stems typically elongate in a limited subapical growth zone, resulting in spatiotemporal correspondence of cell age (since leaving the meristem), growth rate, and developmental state with position along the growing axis (Green, 1976). This dynamic process is properly quantified by growth kinematics, a conceptual framework based on fluid dynamics and continuum mechanics (Silk, 1984; Bastien et al., 2016). The process has been likened to a fountain: a fluid structure that is stable despite a continuous flow of materials through the growth zone. As cells are displaced out of the apical meristem, they enter a region of peak elongation rate and subsequently are displaced out of the elongation zone, ceasing growth and developing characteristics of mature cells. Kinematics shows that the entrance of a cell into the peak growth zone is much slower than its exit, which may be quite abrupt, as short as minutes, depending on the growth rate profile along the axis.

Although this dynamic growth process has long been recognized (Erickson and Sax, 1956), the physiological basis for differences in growth rate along the axis has not been resolved. Spatial gradients in growth hormones (auxin and GA) were proposed (Went and Thimann, 1937; Sánchez-Bravo et al., 1992; Band et al., 2012), but hormones are several steps removed from the biochemical and biophysical processes that drive cell growth (e.g. cell wall loosening and stress relaxation, leading to water uptake and concomitant expansion of the cell wall; Cosgrove, 2016). In previous studies of the maize (*Zea mays*) root, which is perhaps the most

---

[1] This research was supported by the Center for Lignocellulose Structure and Formation, an Energy Frontier Research Center funded by the U.S. Department of Energy, Office of Science, Basic Energy Sciences under Award DE-SC0001090. SANS studies on Bio-SANS by S.V.P. and H.O. were supported by the OBER-funded Center for Structural Molecular Biology (CSMB) under Contract FWP ERKP291, using facilities supported by the Office of Basic Energy Sciences, U.S. Department of Energy.

[2] These authors contributed equally to the article.

[3] Current address: Department of Chemistry, Louisiana State University, Baton Rouge, LA 70809.

[4] Address correspondence to meihong@mit.edu or dcosgrove@psu.edu.

The author responsible for distribution of materials integral to the findings presented in this article in accordance with the policy described in the Instructions for Authors (www.plantphysiol.org) is: Daniel J. Cosgrove (dcosgrove@psu.edu).

P.P., T.W., and M.H. performed the solid-state NMR experiments; S.N.K. and D.J.C. performed the growth and mechanical measurements, monosaccharide analysis, and prepared ^{13}C-enriched cell walls; H.O. and S.V.P. carried out neutron-scattering experiments; all authors contributed to the experimental design, data interpretation, and writing of the article; M.H. and D.J.C. supervised the project.

[OPEN] Articles can be viewed without a subscription.

www.plantphysiol.org/cgi/doi/10.1104/pp.17.01270

intensively studied material for growth kinematics, the spatial pattern of growth rate did not correspond to patterns for wall elastic modulus (Beusmans and Silk, 1988) or cell turgor pressure (Spollen and Sharp, 1991), implying an underlying spatial pattern of wall loosening and relaxation distinctive from wall mechanics and turgor. The basis for growth gradients in shoots has been examined by other approaches. Cell wall creep assays showed that the apical, rapidly growing regions of cucumber (*Cucumis sativus*) hypocotyls and coleoptiles are more responsive than nonelongating regions to the wall-loosening action of exogenous expansins (McQueen-Mason et al., 1992; Cosgrove and Li, 1993), potentially as a result of changes associated with pectin esterification (Zhao et al., 2008). This ties in with other studies implicating pectin deesterification in the decline of growth potential in basal regions of mung bean (*Vigna radiata*) hypocotyl (Goldberg and Prat, 1982).

Here, we have revisited this question, making use of the young inflorescence stem of Arabidopsis (*Arabidopsis thaliana*), with a focus on cell wall polymer mechanics, structure, composition, and dynamics along the growth zone. Recent work has pointed to the advantages of the Arabidopsis inflorescence stem, which is readily marked for growth analysis and provides a powerful system for studying cell development (Suh et al., 2005; Hall and Ellis, 2012). We find that the inflorescence stem also is amenable to mechanical tests, to analysis of wall structure by small-angle neutron scattering (SANS), and to ^{13}C enrichment, enabling high-resolution, multidimensional magic-angle-spinning (MAS) solid-state NMR (SSNMR) spectroscopy to examine wall polysaccharide structures and dynamics along the growth zone, with minimal disruption of cell walls. By enriching cell walls with ^{13}C and studying them in their hydrated, unextracted state, we previously characterized the chemical linkages, conformations, intermolecular interactions, and nanosecond-to-microsecond motions of polysaccharides in cell walls from seedlings grown in shaker flasks containing ^{13}C-enriched Glc (Dick-Pérez et al., 2011; White et al., 2014; Wang et al., 2016b). In this study, we produced ^{13}C-enriched inflorescences by enclosing plants in an atmosphere supplemented with $^{13}CO_2$. Our results identify coordinated changes in cell growth rates, wall mechanics, and wall polysaccharide structures and dynamics, particularly for pectins, along the elongation gradient of the inflorescence stem.

RESULTS

Growth Distribution along the Inflorescence Stem

Under our growth conditions, Arabidopsis inflorescences began to emerge ~28 d after germination. At early stages (less than 4 cm), the entire stem elongated; later, the basal region ceased elongation. This evolution in elongation pattern resembles that of Arabidopsis hypocotyls, where elongation is spatially delocalized at early times and later becomes localized to the apical region (Bastien et al., 2016). For inflorescence stems 5 to 6 cm long, elongation was slightly faster in the light compared with the dark (mean of 1.13 versus 0.94 mm h^{-1}, SE = 0.04; n = 20–23); consequently, our measurements and sample collections were made during the light period. The relative rate of elongation was maximal in the apical region and decreased in a basipetal gradient over ~4 cm (Fig. 1, A and B). This

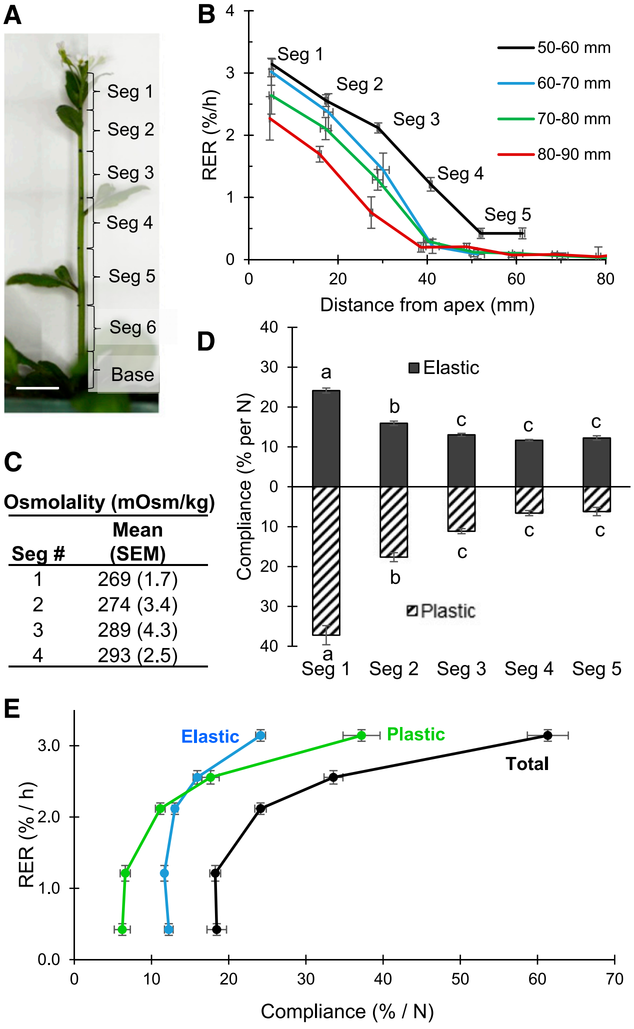

Osmolality (mOsm/kg)

Seg #	Mean (SEM)
1	269 (1.7)
2	274 (3.4)
3	289 (4.3)
4	293 (2.5)

Figure 1. Distribution of elongation rate and other parameters along the Arabidopsis inflorescence stem. A, Photograph of a marked inflorescence with identification of segment numbers. Bar = 1 cm. B, Relative elongation rate (RER) as a function of stem position. Distance values for each segment are calculated as the average of the starting and ending midpoints (mean ± SE; n = 24). C, Osmolality of cell sap expressed from segments #1 to #4 (mean and SE; n = 5). D, Elastic and plastic compliances based on stress/strain analysis of cell walls from 1-cm stem segments along the axis (mean ± SE [units = % strain per N]; $11 < n < 17$). Letters designate statistically significant differences in each series, at $P < 0.01$ (or $P < 0.05$ for comparison of plastic compliances for segment #2 versus segment #3), based on ANOVA and Tukey's test. E, Plot of growth rate against plastic, elastic, and total compliances.

spatial pattern was maintained in older (taller) stems, although growth rate declined slightly as the stem elongated.

For further analysis, we focused on 1-cm segments designated #1 to #4 from stems that were 5 to 6 cm long (Fig. 1A). This set of materials represented cells varying ~3-fold in growth rate (Fig. 1B) but excluded nonelongating regions (i.e. before secondary cell wall production became dominant). The osmolality of cell sap expressed from the four segments was ~280 mosmol kg^{-1} and did not decline along the growth gradient (Fig. 1C). Thus, the growth gradient along the stem was evidently not the result of declining turgor pressure, as solutes actually accumulated slightly in the growing cells despite dilution by water uptake during cell enlargement. Cross sections taken at 1-cm intervals along the stem revealed the same anatomical appearance, with lignin present in the xylem at low but similar levels throughout the elongating region (Supplemental Fig. S1). Estimates of wall thickness, based on wall mass per unit length, did not vary along the growth gradient (see "Materials and Methods"). From these results, we conclude that the differences in growth rate in the elongation zone result from differences in wall extensibility, which depends on biochemical loosening and viscoelastic compliances of the cell walls (Cosgrove, 2016).

To assess viscoelastic compliances along the stem, segments #1 to #4 were frozen, thawed, and mechanically extended in two consecutive cycles (Cosgrove, 2011). The apical stem segments displayed a remarkable ability to stretch, by more than 30% (Supplemental Fig. S2), with the extent of irreversible (plastic) deformation dependent on the applied force. From the slopes of the two force-extension curves, we calculated plastic and elastic compliances (fractional strain per unit of force; reciprocal of stiffness). Both compliances decreased monotonically in a basipetal gradient (Fig. 1D). A plot of growth rate versus compliance shows a strikingly nonlinear relationship (Fig. 1E). Compliances decreased steeply in the apical region and plateaued midway through the elongation zone. The plateau in elastic compliance is particularly notable.

The decrease in wall compliances along the elongation zone could result from changes in polysaccharide structures or from increased binding and cross-linking of these components. Therefore, we assessed the polysaccharide composition of segments #1 to #4 by monosaccharide analysis of the matrix and cellulose components of the wall, using hydrolysis by methanolysis combined with 2 M trifluoroacetic acid (TFA) to distinguish these two components of the wall (Table I). Pectin content (Table II) was highest in apical segment #1 and declined along the growth gradient (60→53 mol %), primarily as a result of decreasing arabinan content (25→18 mol %). Xyloglucan (XyG) content showed a reciprocal pattern, increasing in a basipetal gradient (17→25 mol %). No significant changes in cellulose content (19 mol %; judged as methanolysis-TFA-resistant glucan) were observed along the growing region. Thus, the inflorescence cell walls are rich in pectins and contain lower amounts of cellulose and XyG.

Cellulose Microfibril Organization Assessment by SANS

To assess changes in cell wall organization along the elongation zone, which can potentially result from the history of wall extension or from new patterns of cellulose deposition, we conducted SANS measurements of cell walls from segments #1 to #4. Whole stem segments were frozen, thawed, washed extensively in 2% SDS to remove cytoplasmic contents, and incubated at the contrast match point for cellulose (35% D_2O), as well as in 100% D_2O, where all wall polymers contribute to scattering. These D_2O match points are used to selectively mask neutron scattering by cellulose or matrix, which varies in density and water content (Martínez-Sanz et al., 2016), thereby highlighting neutron scattering by selected components. The scattering intensity is plotted as a function of inverse length (Q; Fig. 2A). The plots for segments #1 and #4 in 100% D_2O are very similar in the low-Q range (0.015–0.1 nm^{-1}, corresponding to 10–67 nm length scale), indicating that the overall architecture of the cell walls changes very little along the elongation zone. In 100% D_2O, both cellulose and matrix polymers contribute to the scattering curves. The similarity of the curves is consistent with the identical appearance of the cross sections along the stem (Supplemental Fig. S1).

In the high-Q (short-length) region of the segment #1 scattering profile, there is a weak, broad peak that

Table I. *Monosaccharide composition as a function of position on the inflorescence stem*

Values are mol % of total sugars (means ± SE; n = 6). The main values in each entry show the sugars, primarily from matrix polysaccharides, released by methanolysis and hydrolysis of the samples with 2 m TFA. The second values, in parentheses, show sugars in the residues (mainly cellulose). Our analysis did not separate Xyl from Man.

Sample	Fuc	Rha	Ara	Gal	Glc	Xyl/Man	GalA	GlcA
Segment #1	2.2 ± 0.1	4.1 ± 0.1	24.7 ± 0.2	19.2 ± 0.3	8.7 ± 0.1 (19.4 ± 0.7)	8.3 ± 0.1 (0.7 ± 0.05)	12.9 ± 0.1	
Segment #2	2.2 ± 0.1	4.3 ± 0.2	19.4 ± 0.5	21.0 ± 0.5	11.0 ± 0.2 (19.4 ± 1.8)	9.6 ± 0.2 (0.8 ± 0.03)	12.2 ± 0.4	
Segment #3	2.2 ± 0.1	4.3 ± 0.1	18.2 ± 0.2	20.6 ± 0.2	11.3 ± 0.1 (19.1 ± 0.4)	10.2 ± 0.1 (1.1 ± 0.04)	13.0 ± 0.3	
Segment #4	2.3 ± 0.1	4.2 ± 0.1	17.6 ± 0.1	19.5 ± 0.2	12.6 ± 0.1 (19.2 ± 0.1)	10.7 ± 0.1 (1.4 ± 0.1)	12.6 ± 0.3	
Base	1.5 ± 0.1	2.9 ± 0.1	10.2 ± 0.2	10.9 ± 0.2	9.4 ± 0.1 (33.0 ± 0.9)	20.1 ± 0.2 (1.9 ± 0.2)	9.8 ± 0.2	0.5 ± 0.1

Table II. *Estimated polysaccharide contents based on sugar analysis*

These data were calculated from Table I using the method described by Wang et al. (2013). Means ± SE; $n = 6$.

Sample	Cellulose	XyG	Xylan + Mannan	Pectin
Segment #1	19.4 ± 0.7	17.3 ± 0.2	2.7 ± 0.1	60.6 ± 0.4
Segment #2	19.4 ± 1.6	21.8 ± 0.4	2.5 ± 0.1	56.3 ± 1.2
Segment #3	19.1 ± 0.4	22.4 ± 0.3	3.1 ± 0.04	55.4 ± 0.2
Segment #4	19.2 ± 0.1	25.1 ± 0.2	2.7 ± 0.1	53.0 ± 0.2
Base	33.0 ± 0.8	18.7 ± 0.2	17.0 ± 0.4	31.3 ± 0.4

becomes slightly more pronounced in the segment #4 profile (Fig. 2B). We can assign this scattering feature to the contribution of cellulose microfibrils, because it disappears in samples measured at the contrast match point of cellulose (35% D_2O; Fig. 2C). The peak maximum is at ~1.52 nm^{-1} in both samples (Fig. 2D); this feature indicates that (1) some cellulose microfibrils are spatially correlated (i.e. aligned) in the wall and (2) the distance between the microfibrils that generate this scattering feature remains unchanged along the elongation zone. Note that unaligned microfibrils do not generate peaks in the scattering curve, so we are focusing here solely on the aligned fraction of the microfibrils. The average distance between two neighboring microfibrils (d), calculated from the peak position using Bragg's law ($d = 2\pi/\text{peak position}$), is ~4.1 nm. However, considering the absence of a sharp Bragg peak in the scattering pattern, a more accurate analysis was performed using the unified fit approach (Table III), which provides a multilevel fit of the scattering data (Beaucage, 1995; Stribeck, 2007; Fig. 2, E and F). The calculated ζ value, which represents the average distance between the correlated particles, is ~3.9 nm for the high-Q (level 1) region, which is similar to the distance obtained directly through Bragg's law (Fig. 2D; Stribeck, 2007). The dimensionless packing parameter (k) obtained from the fit is indicative of how well the system is ordered (Beaucage et al., 1995). The upper limit (k = 5.92) indicates a perfect hexagonal or face-centered cubic crystal structure, and k decreases to zero in an uncorrelated system. In this study, intermediate k values of 2.2 and 3.2 were obtained for segments #1 and #4 (Table III), respectively, indicating an increased alignment of the microfibrils along the elongation zone.

These SANS profiles indicate that cellulose is not strongly aligned in the primary walls of the inflorescence and changes very little along the elongation zone, other than a slight increase in alignment. This is a remarkable observation, considering the large extent of cell wall elongation as cells are displaced from the top of segment #1 to the bottom of the elongation zone (estimated to be ~6-fold by kinematic analysis). We interpret the correlation distance (ζ) in the high-Q range as arising from close lateral packing of cellulose microfibrils in limited regions of microfibril bundling, as seen in onion (*Allium cepa*) cell walls (Zhang et al., 2016). We also note that the ζ value obtained from the unified fit analysis is similar to the microfibril diameter (~3.5 nm), indicating that the correlations observed in the scattering profile are primarily between neighboring pairs of microfibrils, with no evidence of a longer range order of microfibrils. This conclusion does not exclude the occurrence of larger bundles of microfibrils, but weak ordering may prevent their resolution in these SANS curves. The increase in the k parameter is interpreted as increased microfibril alignment of the paired microfibrils along the growth zone. Finally, the increase in the power-law exponent from 2.54 to 2.74 at low Q (level 3; 0.015–0.1 nm^{-1}) may be due to an increase in the density, packing, or entanglement of matrix polymers, perhaps as a consequence of cell wall extension or changes in matrix polysaccharides, evidenced in the composition analysis described above and further confirmed by the SSNMR data shown below.

Polysaccharide Composition and Dynamics from 1D ^{13}C SSNMR Spectra

To investigate the wall polysaccharide structures and dynamics of the growing inflorescence stem at the molecular level, we prepared cell walls from plants grown in an atmosphere containing ^{13}C-enriched CO_2, thereby enabling 2D ^{13}C SSNMR experiments. We first examined the polysaccharide composition of cell walls from inflorescence segment #1 using quantitative ^{13}C direct polarization (DP) experiments (Fig. 3A). The ^{13}C spectrum is dominated by many well-resolved matrix polysaccharide peaks with line widths of 0.3 to 0.6 ppm (Wang et al., 2015). Many of these sharp signals can be assigned to pectins, such as the 108-ppm Ara C1 peak, the Rha and GalA signals at 101, 79, and 69 ppm, the 53.5-ppm methyl ester signal, and the 21-ppm acetyl signal of rhamnogalacturonan-I (RG-I). Three carbonyl peaks are observed at 172, 174, and 176 ppm and can be assigned to GalA methyl ester in homogalacturonan (HG), GalA acetyl, and GalA carboxylate in RG-I and HG, respectively (Wang et al., 2016a). The cellulose intensities in these inflorescence cell walls are much lower than those of seedling cell walls, as seen for the resolved interior cellulose C4 peak at 89 ppm and the C6 peak at 65 ppm (Dick-Pérez et al., 2011). No lignin signals are detected, as evidenced by the absence of the OCH_3 methoxy signal at 56 ppm. Thus, the cell walls of fast-growing segment #1 have a high pectin content and low cellulose content.

We next probed polysaccharide dynamics by a series of ^{13}C NMR experiments that selectively detect molecular segments with different mobilities. The ^{13}C cross-polarization (CP) experiment preferentially enhances the signals of rigid molecules. The spectrum shows significantly higher 89- and 65-ppm intensities of interior cellulose C4 and C6 (Fig. 3B) than the quantitative spectrum. In addition, several overlapping peaks in the quantitative DP spectrum, which have a superposition of broad and narrow line shapes, retain only the broad component in the CP spectrum, indicating that the

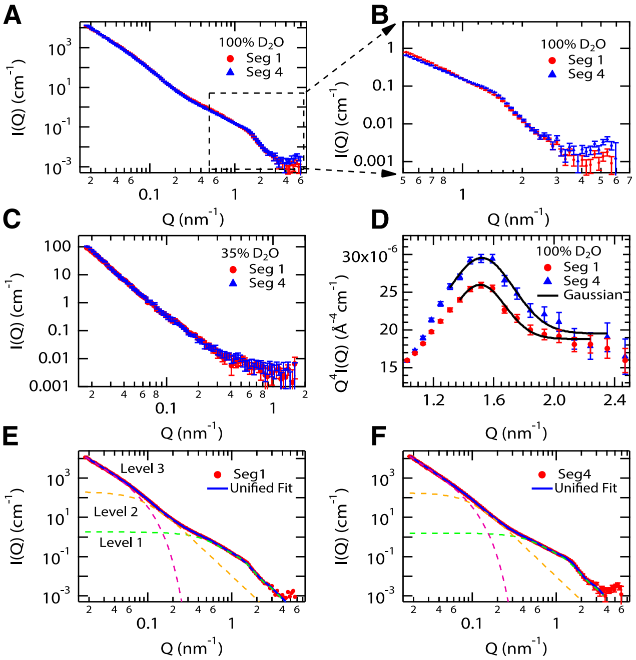

Figure 2. SANS analysis of inflorescence stem segments. A, SANS profiles for segments #1 and #4 in 100% D_2O. B, SANS profiles for segments #1 and #4, highlighting differences in the high- and mid-*Q* ranges. C, SANS curves for segments #1 and #4 measured at the contrast match point for cellulose (35% D_2O). D, $Q^4I(Q)$ versus *Q* representation of the high-*Q* region of SANS profiles for segment #1 (red) and segment #4 (blue) in 100% D_2O. A Gaussian fit to the curves (solid black line) yielded a peak position of 1.52 nm^{-1} for both curves. E and F, SANS data of stem segment #1 (E) and segment #4 (F). The unified fit curves are shown as a solid black line in each plot. The three fit levels are presented as dashed green (level 1), gold (level 2), and magenta (level 3) lines.

intensities of the dynamic matrix polysaccharides have been suppressed by CP. Examples include the 105-ppm C1 peak of interior cellulose, surface cellulose, Gal, and the Glc backbone of XyG and the 84-ppm C4 peak of surface cellulose and Ara. The arabinan signals at 108, 84, and 82 ppm are completely suppressed in the CP spectrum, while a significant fraction (~85%) of Rha and GalA signals remains. Thus, the pectin backbones (HG and RG-I) are less mobile than the Ara and Gal side chains.

Complementing the CP spectrum, a ^{13}C DP spectrum was measured using a short recycle delay of 2 s to selectively detect mobile molecules (Fig. 3C). The spectrum shows both pectin backbone and side chain signals and has similar overall intensity distributions to the quantitative spectrum, supporting the conclusion that the segment #1 cell wall has low amounts of cellulose and XyG. Finally, we measured a ^{13}C spectrum where the ^{13}C polarization is transferred from ^{1}H spins via ^{1}H-^{13}C scalar coupling using the INEPT (insensitive nuclei enhanced by polarization transfer) experiment. A 6-ms mixing time was used for ^{1}H-^{13}C coherence transfer, during which no ^{1}H-^{1}H homonuclear dipolar decoupling was employed. Thus, the magnetization of rigid polysaccharides with strong ^{1}H-^{1}H dipolar couplings is suppressed in the INEPT spectrum. Among the four experiments, the INEPT experiment (Fig. 3D) has the highest selectivity for dynamic molecules and manifests the highest spectral resolution, with no residual broad line shapes. Most pectin backbone Rha and GalA signals are suppressed, leaving predominantly Ara and Gal side chain intensities. The INEPT ^{13}C spectrum shows high resolution at 105, 70 to 75, and 62 ppm and exhibits multiple sets of Ara and Gal signals (vide infra). The unprotonated carbonyl and carboxyl signals are suppressed due to the lack of directly bonded protons.

Faster Growing Inflorescence Cell Walls Have More Branched Pectins

To assess how the polysaccharide composition of the inflorescence cell wall differs along the growth gradient and differs from cell walls of seedlings (Wang et al., 2015), we compared the quantitative ^{13}C spectra of the four inflorescence samples and the previously reported seedling cell wall (Fig. 4). To account for differences in sample amount, we normalized each spectrum by its total integrated intensity, excluding the 25- to 30-ppm lipid region. Figure 4 compares the normalized spectra of the five cell walls. Several important features are observed. First, cellulose intensities increase moderately from inflorescence #1 to #4 (see different spectra in Supplemental Fig. S3), but all four inflorescence segments have notably lower cellulose contents (estimated from these spectra to be 38%–49%) than the seedling cell wall. In contrast, pectin intensities decrease from inflorescence #1 to inflorescence #4 but are still distinctly higher than that of the seedling cell wall. Second, pectin side chain signals decrease more strongly than pectin backbone signals from segments #1 to #4, as seen by the relative intensities of the 108-ppm Ara C1 peak, the 101-ppm Rha and GalA C1 peak, and the 17-ppm Rha C6 peak. Third, the methyl ester and acetyl peak intensities at 54, 172, 21, and 174 ppm decrease by 5% to 15% from segments #1 to #4, while the 176-ppm carboxyl peak increases by ~6%. Therefore, esterified and nonesterified GalA C6 exhibit opposite and correlated intensity changes along the elongation zone. These observations extend the data of Tables I and II, showing that, compared with segment #4, the cell wall of the fastest growing segment #1 has higher pectin and slightly lower cellulose contents, more extensive side chain branching, and a higher degree of methyl esterification and acetylation.

To fully resolve the matrix polysaccharide signals and compare them between the inflorescence and seedling cell walls, we measured 2D ^{13}C-^{13}C DP-based J-INADEQUATE spectra, which correlate the sum chemical shifts of two directly bonded carbons with their individual chemical shifts (Dick-Pérez et al., 2011). The 2D ^{13}C-^{13}C J-INADEQUATE spectra were measured using direct ^{13}C polarization and a short recycle delay of

Table III. *Structural parameters of segments #1 and #4 in 100% D_2O calculated from fitting with the unified fit model*

Sample	Structural Level (Length Scale)[a]	Q Range	Radius of Gyration (R_g)	Power-Law Exponent (P)[b]	Correlation Distance (ζ)	Degree of Correlation (k)
		nm⁻¹	*nm*		*nm*	
Segment #1	1 (0.8–6.3 nm)	0.5–4	3.9 ± 0.14	*4	3.96 ± 0.11	2.2 ± 0.8
	2 (6.3–31.4 nm)	0.1–0.5	21.2 +2.5/−1.7	*4		
	3 (31.4–104 nm)	0.03–0.1		2.54 ± 0.04		
Segment #4	1 (0.8–6.3 nm)	0.5–4	3.7 ± 0.15	*4	3.92 ± 0.08	3.2 ± 0.6
	2 (6.3–31.4 nm)	0.1–0.5	20.0 +2.8/−2.3	*4		
	3 (31.4–105 nm)	0.03–0.1		2.74 ± 0.03		

[a] Numbers in parentheses are estimates of the real-space ranges calculated using the relationship π/Q (nm^{-1}). [b] Asterisks denote parameters that were fixed during the fit process.

2 s to preferentially detect the signals of mobile polysaccharides. The inflorescence spectrum shows predominantly pectin signals, with line widths of 0.3 to 0.8 ppm, with no detectable cellulose signals and minimal XyG signals (Fig. 5A; Supplemental Fig. S4). In comparison, the seedling cell wall exhibits residual cellulose intensities and stronger XyG correlation signals, such as the x1-x2 peaks at the double-quantum chemical shift of 172 ppm and the x4-x5 peaks at the 133-ppm cross section. In addition, the spectra of the inflorescence cell walls resolve multiple forms of pectins, some of which are not found in the seedling. At least five sets of Ara and Gal signals and four sets of GalA resonances can be resolved in inflorescence cell walls (Fig. 5B; Table IV). Among the five sets of α-L-Ara signals (Zykwinska et al., 2005), type a and type b Ara are unique to the inflorescence cell walls and absent in the seedling. Type a Ara shows a downfield C2 chemical shift of 87.8 ppm, indicating 2,5-linked α-L-Ara, while type b Ara exhibits downfield C2 and C3 chemical shifts of 85.8 and 81.1 ppm, suggesting 2,3,5-linked α-L-Ara. Similarly, Ara-c and Ara-d can be assigned to 5-α-L-Ara and t-α-L-Ara, respectively, and are also present in seedling cell walls. Additionally, seedling cell walls show relatively low Ara-f content, a 2,5-linked α-L-Ara. Figure 5C summarizes the structures of the four assigned α-L-Ara linkages found in the inflorescence cell walls. The Ara structural diversity is reminiscent of the *Brachypodium distachyon* primary cell wall (Wang et al., 2014), although the latter does not contain 2,5- and 2,3,5-linked Ara. The

Figure 3. ^{13}C MAS spectra of inflorescence segment #1 at 298 K. A, Quantitative ^{13}C DP spectrum measured with a 30-s recycle delay. B, ^{13}C CP spectrum. C, ^{13}C DP spectrum measured with a 2-s recycle delay. D, ^{13}C INEPT spectrum, which detects only the signals of extremely mobile segments. Spectra are plotted to scale with the number of scans. Assignment is given as the carbon number preceded by one- to three-letter codes of the monosaccharides, whose abbreviations are shown at the top right corner.

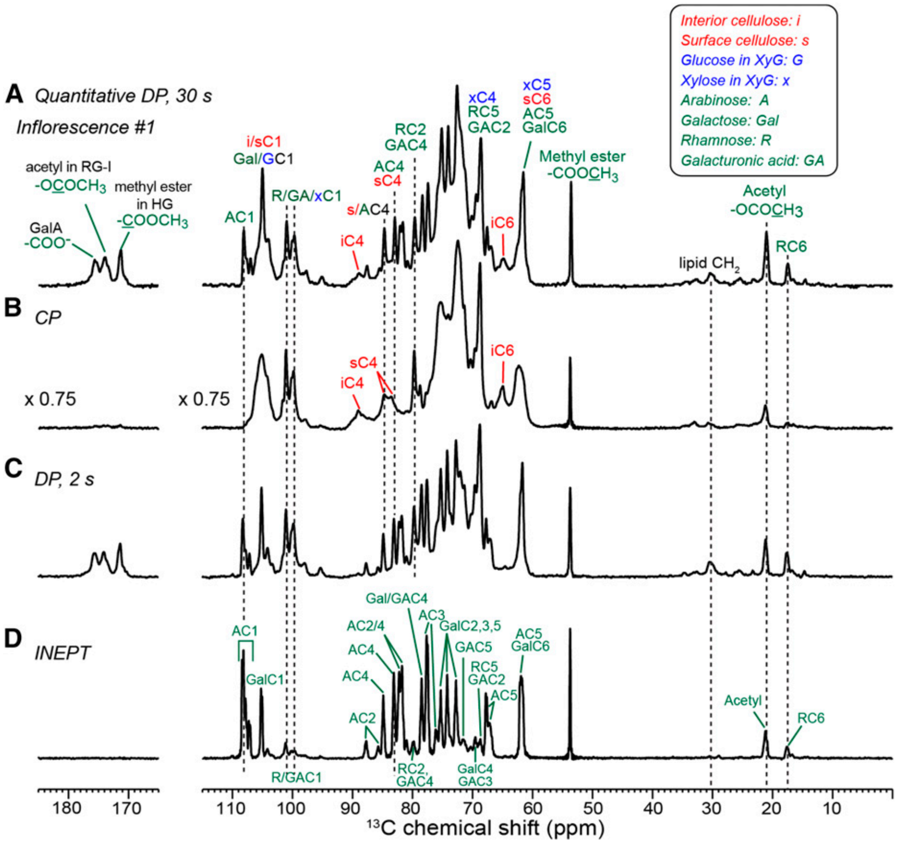

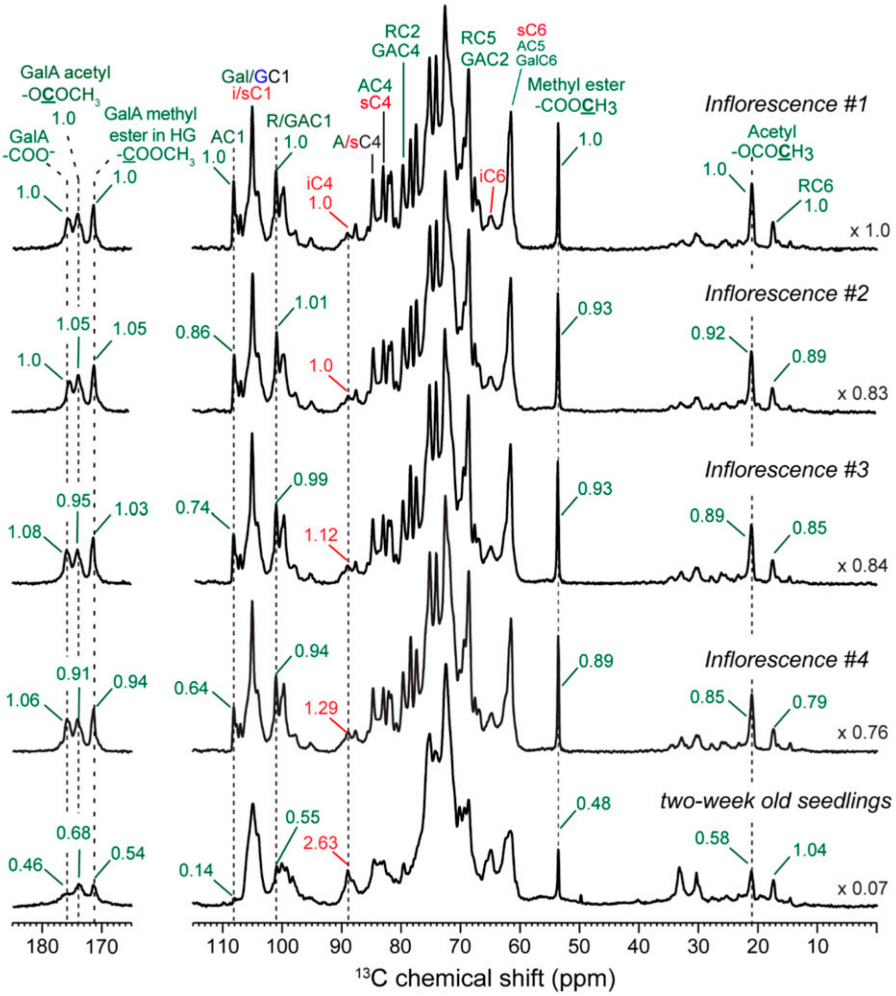

Figure 4. Quantitative ^{13}C DP spectra of inflorescence segments #1 to #4 and never-dried cell walls of seedlings grown in shaker flasks. Each spectrum is normalized by the integrated intensities of the whole spectrum to account for sample amount differences. The scaling factor for normalization is indicated on the right. Pectin signal intensities decrease while cellulose intensities increase from segments #1 to #4, and Ara signals decrease more strongly than pectin backbone Rha and GalA signals. The seedling cell wall has significantly more cellulose, less pectins, and less pectin side chain branching than all inflorescence samples.

inflorescence cell walls exhibit three Rha signals that are also present in seedling cell walls, while a fourth Rha in seedlings is absent in the inflorescence samples (Fig. 5B). Finally, unlike the *B. distachyon* cell walls, these Arabidopsis inflorescence walls do not show detectable xylan signals. Figure 5D compares the xylan regions in the DP-J-INADEQUATE spectrum of the *B. distachyon* cell wall (Wang et al., 2014) with the same regions of the inflorescence #1 spectrum, showing a clear absence of xylan signals in the inflorescence spectra, in good agreement with the monosaccharide analysis (Tables I and II). These data, taken together, show that inflorescence cell walls contain more dynamic pectins with increased Ara side chain branching as well as distinct backbone conformations of RG-I and HG.

Inflorescence Cell Walls Have Strong Water-Polysaccharide Interactions

Our previous SSNMR spectra of seedling cell walls showed that calcium cross-linked HG is important for maintaining wall hydration by trapping and partially immobilizing water (White et al., 2014; Wang et al., 2015). To investigate how water interacts with the pectin-rich inflorescence cell walls, we measured 2D ^{1}H-^{13}C heteronuclear correlation (HETCOR) spectra. To resolve the water and polysaccharide ^{1}H chemical shifts, we added a ^{13}C dipolar dephasing period to the standard HETCOR pulse sequence to suppress the polysaccharide ^{1}H signals while retaining only the water ^{1}H signal (Yao and Hong, 2001). As for the HETCOR experiment, the medium- and long-distance (MELODI)-HETCOR experiment utilized ^{1}H-^{13}C CP for polarization transfer, thus preferentially detecting rigid segments with large dipolar couplings. Figure 6A shows the 2D MELODI-HETCOR spectrum, where water cross peaks with relatively rigid polysaccharides are readily observed at the ^{1}H chemical shift of 4.7 ppm. Due to the CP transfer, the MELODI-HETCOR experiment suppresses the signals of mobile segments, such as the 108-ppm Ara C1 peak and the 54-ppm methyl ester peak, even if these segments are well hydrated. To compare the hydration levels of the different cell walls, we compared the intensities of the water-transferred ^{13}C signals in the 2D

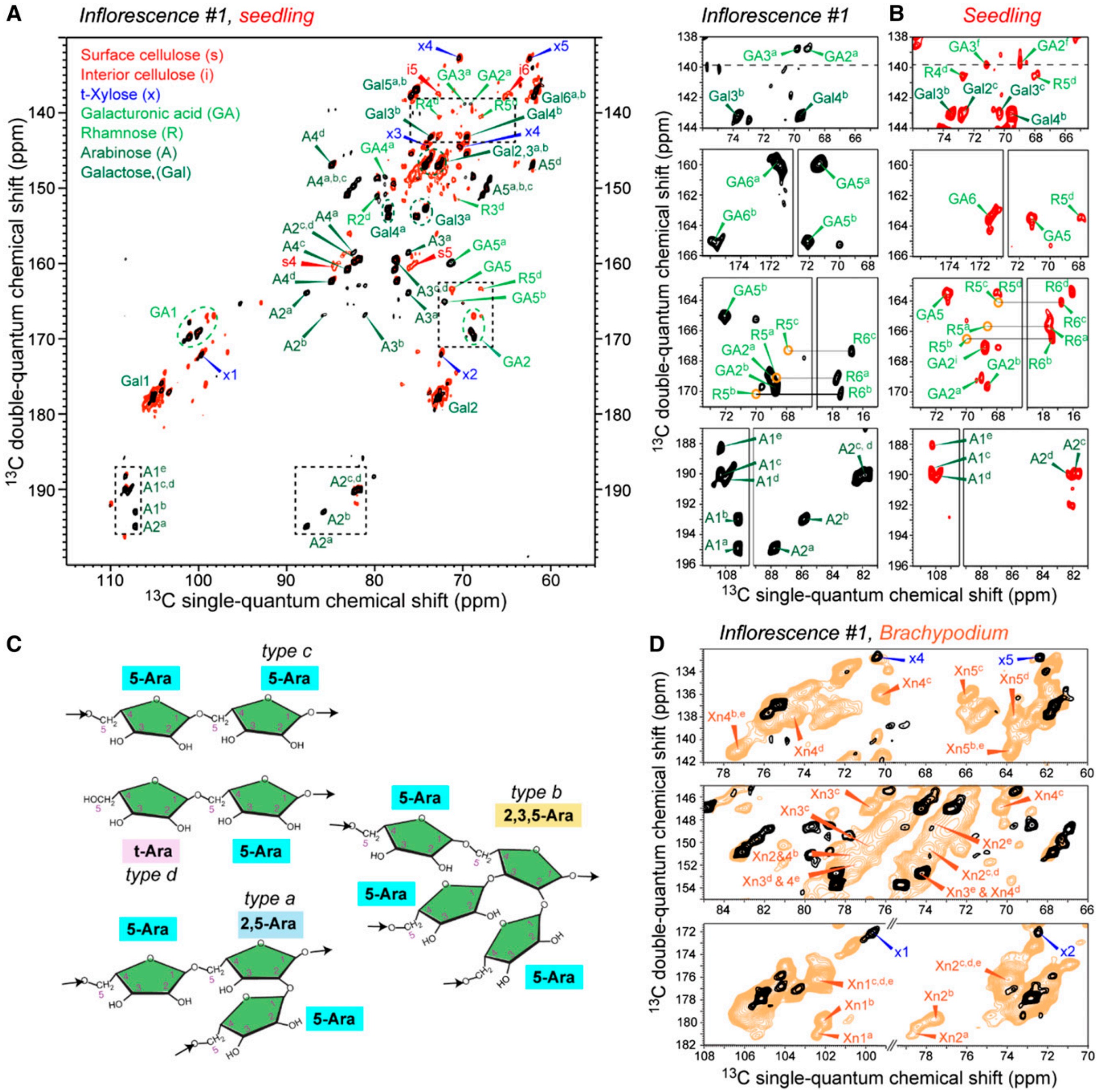

Figure 5. A, 2D ^{13}C DP-based J-INADEQUATE spectrum of inflorescence #1 (black) overlaid with the spectrum of seedling cell walls (red). The spectra were measured using direct ^{13}C polarization and a short recycle delay of 2 s to preferentially detect the signals of mobile polysaccharides. α-L-Ara signals are observed in both inflorescence and seedling cell walls. The inflorescence cell wall shows highly branched 2,5-linked α-L-Ara (type a) and 2,3,5-linked α-L-Ara (type b) signals, which are absent in the seedling cell wall. Assignment superscripts indicate the different linkages and conformations within each sugar. The ω_1 spectral widths are 82.7 and 79.4 ppm for inflorescence #1 and seedling cell walls, respectively. The GA carbonyl and Rha C6 signals are folded in the ω_1 dimension. B, Selected regions of the 2D spectra showing the resolution of multiple types of Ara, GalUA, Gal, and Rha signals. Orange circles indicate missing Rha C5 cross peaks, whose chemical shifts are unambiguous based on the observed Rha C6 chemical shifts. C, Representative structures of 2,5-Ara^a, 2,3,5-Ara^b, 5-Ara^c, and t-Ara^d observed in the inflorescence cell walls. D, Selected regions of the inflorescence #1 INADEQUATE spectrum (black) overlaid with a previously measured *B. distachyon* spectrum (orange). *B. distachyon* cell walls exhibit abundant xylan (Xn) signals, which are absent in the Arabidopsis inflorescence cell wall.

Table IV. *^{13}C chemical shifts of inflorescence primary wall matrix polysaccharides compared with chemical shifts found in the cell walls of 2-week-old seedlings for selected sugars*

Residue	Linkage	Cell Walls	C1	C2	C3	C4	C5	C6
			ppm					
Ara^{a}	2,5-Ara	Inflorescence	107.2	87.8	76.2	82.4	67.3	–
Ara^{b}	2,3,5-Ara	Inflorescence	107.2	85.8	81.1	81.9	67.0	–
Ara^{c}	5-Ara	Both	108.4	81.8	77.8	83.1	67.8	–
Ara^{d}	t-Ara	Both	107.7	82.2	77.5	84.9	62.1	–
Ara^{e}	–	Both	108.3	80.1	–	–	–	–
Ara^{f}	2,5-Ara	Seedlings	108.5	88.0	–	–	–	–
Ara^{h}	–	Seedlings	109.9	82.0	–	–	–	–
Xyl	t-Xyl	Both	99.7	72.5	74.0	70.4	62.4	–
Gal^{a}	4-Gal	Both	105.2	72.8	74.3	78.5	75.3	61.7
Gal^{b}	t-Gal	Both	105	72.3	73.7	69.6	75.8	61.9
Gal^{c}	–	Both	104.2	72.5	–	–	–	–
Gal^{d}	–	Both	103.4	73.6	–	–	–	–
Gal^{e}	–	Both	104.2	71.6	–	–	–	–
Gal^{f}	–	Seedlings	ND	72.5	70.2	–	–	–
GalA^{a}	4-GalA	Inflorescence	99.9	69.0	69.8	78.8	71.3	171.6
GalA^{b}	–	Both	101	68.7	–	–	72.1	175.8
GalA^{c}	–	Inflorescence	101.7	68.6	–	–	–	–
GalA^{d}	–	Both	101	66.8	–	–	–	–
GalA^{e}	–	Seedlings	100.2	69.3	–	–	–	–
GalA^{f}	–	Seedlings	100.1	68.9	71.1	–	–	–
GalA^{g}	–	Seedlings	99.1	67.9	–	–	–	–
GalA^{h}	–	Seedlings	99.0	68.6	–	–	–	–
GalA^{i}	–	Seedlings	98.4	68.8	–	–	–	–
Rha^{a}	–	Both	–	–	–	–	68.7	17.8
Rha^{b}	–	Both	–	–	–	–	70.1	17.4
Rha^{c}	–	Both	–	–	–	–	67.9	16.8
Rha^{d}	2-Rha	Seedlings	ND	79.8	71.0	72.7	68.0	16.1

ND, Not determined; –, not identified.

MELODI-HETCOR spectrum with the full ^{13}C intensities in the 1D CP spectra. Figure 6B shows that inflorescence segment #1 has higher water-transferred pectin ^{13}C intensities than segment #4, and both cell walls have higher water-transferred ^{13}C intensities than seedling cell walls. Therefore, the fastest growing segment #1, which has the highest pectin content and esterification, also has the strongest water-polysaccharide interactions. 1D ^{1}H spectra show that the water ^{1}H line width is broader (0.32 ppm) in the inflorescence #1 cell wall than in the seedling cell wall (0.12 ppm; Fig. 6C), indicating that water is more immobilized by polysaccharides of the growing inflorescence stem.

Inflorescence Wall Polysaccharides Have Distinct Mobilities

To quantify the polysaccharide mobilities in inflorescence cell walls, we measured ^{13}C-^{1}H dipolar order parameters (S_{CH}) using the dipolar chemical-shift correlation (DIPSHIFT) experiment, which detects the amplitude of reorientational motions of C-H bonds on the submicrosecond time scale. For cellulose, CP-based DIPSHIFT experiments indicated similar order parameters of greater than 0.9 for cellulose in both inflorescence and seedling cell walls (Fig. 7; Supplemental Fig. S5), indicating that cellulose microfibrils are immobilized, as expected. In comparison, quantitative ^{13}C DIPSHIFT experiments show different pectin mobilities for the different cell walls: segment #1 exhibits smaller S_{CH} values and, thus, higher mobility than segment #4, while both segments have more dynamic pectins than seedling cell walls. The CP-DIPSHIFT spectra display a similar trend. Since the CP-DIPSHIFT experiment preferentially detects the more rigid pectins that are in contact with cellulose, this mobility trend indicates that pectin backbones that are in contact with cellulose microfibrils are increasingly rigidified in the apical-to-basal direction, suggesting stronger interactions with cellulose microfibrils.

We also measured ^{1}H rotating-frame spin-lattice relaxation times ($T_{1\rho}$) to probe the motional rates of polysaccharides on the microsecond time scale. Compared with the seedling cell wall, the inflorescence cell walls have similar cellulose $T_{1\rho}$ values but longer pectin $T_{1\rho}$ values (Supplemental Fig. S6). These pectin ^{1}H $T_{1\rho}$ values decrease with decreasing temperature, indicating that the pectin motional rates are faster than the characteristic time scales of ~16 μs. Thus, the longer relaxation times of pectins in inflorescence compared with seedling cell walls indicate faster pectin motions.

Figure 6. 2D ^{1}H-^{13}C correlation spectra to investigate polysaccharide hydration. A, 2D MELODI-HETCOR spectrum of inflorescence #1 measured using a 1-ms ^{1}H spin diffusion and Lee-Goldburg CP polarization transfer, which suppresses highly dynamic signals, such as the 108-ppm Ara C1 peak and the 54-ppm methyl ester signal. B, Comparison of the water cross sections of the MELODI-HETCOR spectra (blue) and the 1D ^{13}C CP spectra (black) of inflorescence #1, inflorescence #4, and seedling cell walls. Intensity ratios are indicated for selected peaks. C, 1D ^{1}H spectra of inflorescence #1 and seedling cell walls, showing a broader water peak and, hence, more immobilized water in the inflorescence cell wall.

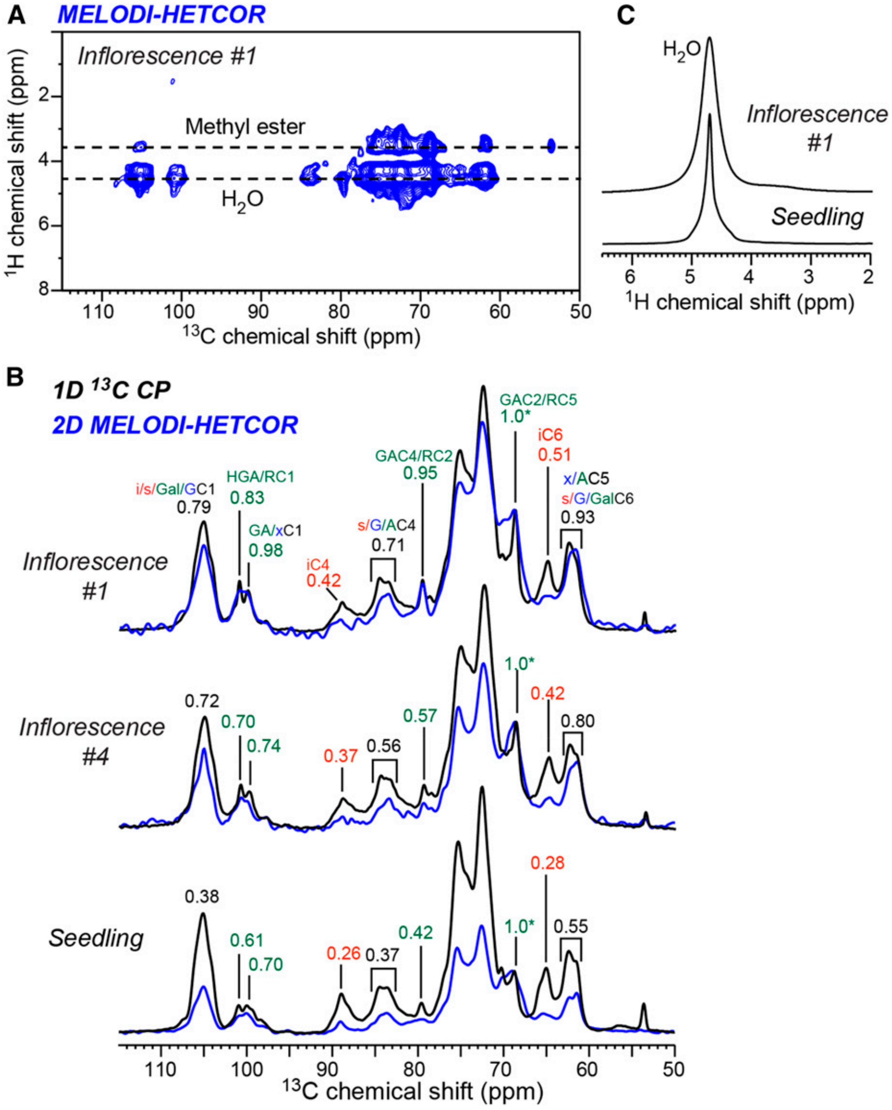

Together, these data indicate that cellulose microfibrils are similarly rigid in inflorescence and seedling cell walls, but pectin mobilities differ, and the apical stem has the most dynamic pectins. Thus, wall polysaccharide dynamics is more heterogenous in the fastest growing inflorescence cell walls, suggesting weaker pectin-cellulose interactions.

DISCUSSION

Our results show that the apical-to-basal decrease in elongation rate along the Arabidopsis inflorescence stem, measured here in relatively young inflorescences and in previous studies in older stems (Suh et al., 2005; Hall and Ellis, 2012), is accompanied by wall stiffening, quantified as decreasing elastic and plastic compliances in stress/strain measurements, and by reduced polysaccharide mobility, weaker water-polysaccharide interactions, less branching, and reduced esterification of pectins, as seen in the SSNMR data. However, as in the case of maize roots (Beusmans and Silk, 1988), the distribution of growth rate did not parallel the distribution of wall compliances along the inflorescence stem. The SANS data indicate rather subtle increases in microfibril alignment and polysaccharide packing density along the elongation zone. From the growth kinematic profile, we calculate that cells increased in cellular volume and lateral wall surface area by 6-fold during the estimated 60-h transit through the ink-marked locations at the starting and ending points of the elongation zone. Thus, it is noteworthy that cell osmotic pressure, and presumably turgor pressure, did not decline along this growth gradient; likewise, wall thickness remained constant. Evidently, passive cell wall thinning and dilution of osmotic pressure during cell elongation are closely matched by active cell wall deposition and generation of osmotic solutes, which

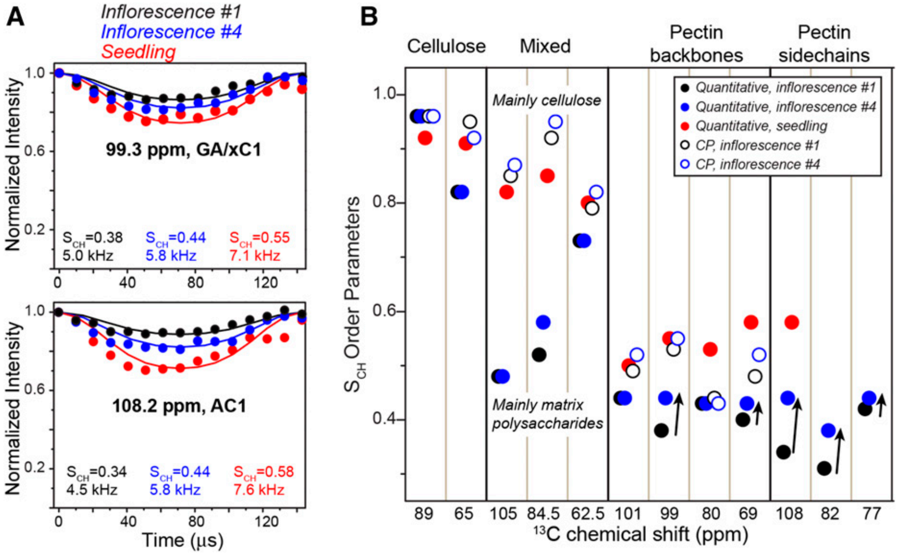

Figure 7. Motional amplitudes of polysaccharides from ^{13}C-^{1}H dipolar couplings. A, Representative quantitative DIPSHIFT curves of inflorescence #1 (black), inflorescence #4 (blue), and seedling (red) cell walls. The best-fit C-H dipolar couplings (with frequency-switched Lee-Goldburg [FSLG] scaling) and the corresponding order parameters (S_{CH}) are indicated. B, S_{CH} values of various polysaccharides, measured using quantitative (closed circles) and CP DIPSHIFT (open circles) experiments. Arrows highlight the increased rigidity of pectins from inflorescences #1 to #4.

can be estimated precisely with kinematic approaches (Silk and Bogeat-Triboulot, 2014). The growing stem cells apparently coordinate growth with these cellular processes more closely than do Arabidopsis hypocotyls (Refrégier et al., 2004), whose cell walls thinned during elongation, or pea (*Pisum sativum*) epicotyls (Cosgrove and Cleland, 1983), whose cell osmotic pressure declined slightly along the elongation zone. The last two examples notwithstanding, plant cell growth is generally well coordinated with the production of cellular materials needed for mechanical stability, and the Arabidopsis inflorescence is a fine example of such coordination.

The decline in cell wall mechanical compliances along the stem implies a change in wall structure, yet we did not detect parallel changes in cellulose structure by SSNMR or SANS, other than a modest increase in cellulose content and microfibril alignment. Whether such subtle changes influence wall mechanics or growth is uncertain at this time. The increased alignment could be the result of wall strain during growth, or changes in matrix polysaccharides, or changes in the wall assembly process at the later stages of stem elongation. In contrast, pectic polysaccharide structure and dynamics showed pronounced changes along the elongation zone, with lower arabinan and galactan content, decreased esterification, reduced pectin mobility, and weaker water-pectin interactions in the apical-to-basal direction. In previous work, decreases in pectin esterification and increases in calcium cross-linking were associated with growth cessation in mung bean hypocotyls (Goldberg, 1984; Goldberg et al., 1986) and with loss of cell wall creep induced by expansins in cucumber hypocotyls (Zhao et al., 2008). Likewise, pectin mobility, as measured by SSNMR spin relaxation, was reduced in pectin-rich collenchyma from nongrowing (tall) stalks of celery (*Apium graveolens*) compared with shorter (still growing) stalks (Fenwick et al., 1997). Our results demonstrate an additional instance of such correlations, with new dimensions to the changes in pectins.

Recently, we demonstrated that interactions between cellulose and pectins, mainly RG-I and a portion of HG backbones, are inherent to plant primary cell walls and not simply a matter of molecular crowding (Wang et al., 2012, 2015). With these studies as background, we suggest that pectin-cellulose interactions increase as cells are displaced through the elongation zone of the inflorescence stem and that a consequence of increased interactions is a decrease in mechanical compliances. These compliances should not be mistaken for measures of wall extensibility in the sense of plant growth, meaning “the ability of the cell wall to increase in surface area irreversibly during growth” (Cosgrove, 2016), a process that requires dynamic wall loosening and stress relaxation. For the stems studied here, growth rate and compliances both decline along the stem, but in highly nonlinear ways (Fig. 1E), which suggests that wall loosening and viscoelasticity may make different contributions to growth along the elongation zone. The stress/strain compliances do not measure wall loosening per se but depend instead on wall structure and, hence, are influenced by the extent of microfibril-microfibril binding (via direct contacts as well as indirect contacts mediated by matrix polysaccharides), the conformation and hydration of matrix polysaccharides (Edelmann, 1995; Evered et al., 2007), and the extent of covalent cross-linking of matrix components (de O Buanafina, 2009). Current concepts of primary cell wall structure have not yet been developed in sufficient detail to predict the dependence of wall mechanics on wall structure, a notable gap in the cell wall field.

Our results show that wall mechanical stiffness increases as pectins lose certain features, implying a mechanical aspect to one or more of these structural changes. This inference is at odds with the common notion that the cellulose scaffold is the principal load-bearing structure in primary cell walls. This idea springs from the high stiffness of cellulose microfibrils but fails to consider how cellulose microfibrils are connected to one another to form a mechanically strong material. A recent study that combined extensometry with atomic force microscopy and different forms of cell wall strain showed that both cellulose microfibrils and matrix polymers, predominantly pectins, bear the tensile load of elastically stretched onion walls (Zhang et al., 2017). This confirms the mechanical significance of the matrix at the molecular scale and adds impetus to recent interest in the state of pectins in growing cell walls and the need for better models of cell wall mechanics (Peaucelle et al., 2012; Xiao et al., 2014; Levesque-Tremblay et al., 2015).

Although pectin-cellulose molecular interactions are evident in SSNMR spectra of cell walls, in vitro binding studies have not replicated comparable interactions. For instance, when incubated at low concentration with various forms of cellulose, neutral pectic side chains (debranched arabinans and galactans) bind to cellulose with low to moderate strength, but the pectic backbones (HG and RG-I) display negligible affinity to cellulose (Chanliaud and Gidley, 1999; Zykwinska et al., 2005, 2007a, 2007b, 2008; Park et al., 2014; Lin et al., 2015). In contrast, 2D ^{13}C-^{13}C correlation SSNMR spectra show cross peaks indicating that pectins in native cell walls interact with cellulose chiefly through their backbones. A molecular understanding of this difference in pectin behavior in vitro versus in vivo is needed. Do distinctive interactions arise from the manner in which cellulose and matrix components are deposited and assembled to make the native wall, with cellulose bundling and matrix entrapment inherent in the process of wall formation (Cosgrove, 2014; Zhang et al., 2016)? Or do pectin differences such as esterification, branching, and concentration result in distinct interactions with cellulose in vivo versus in vitro? Is the change in mechanical stiffness along the stem the result of different assembly of the cell wall as the cells progress through the elongation zone, or does the preexisting cell wall change in concert with the newly deposited cell wall, as pectin is modified by wall enzymes such as esterases and glycosidases? Future work with the Arabidopsis inflorescence stem, with its natural gradient in wall mechanics and pectin properties, may provide answers to these questions.

MATERIALS AND METHODS

Growth and ^{13}C Labeling of Inflorescence Cell Walls

Following 3 d of cold treatment, seeds of Arabidopsis (*Arabidopsis thaliana*), ecotype Columbia-0, were germinated for 1 week on 1× Murashige and Skoog basal salts (Sigma-Aldrich; no. M5524) with 1% Suc, then transferred to potting soil (Promix BX) and grown in a chamber programmed for a 12-h-light/12-h-dark photoperiod (22°C/16°C) at 120 to 150 μmol m^{-2} s^{-1} light intensity. For growth analysis, plants were selected by height of the inflorescence stems, which were marked by hand with oil-based ink at 1-cm increments, with the topmost mark placed just below the point where the floral clusters emerged from the stem. Stems were photographed at the start of the light period and 10 h later. Relative elongation rates for each segment were calculated as [ln(final length) − ln(initial length)]/Δtime. For osmolality measurements, cell sap was expressed from frozen and thawed stem segments from segments #1 to #4 and measured in a vapor pressure osmometer (Wescor; model no. 5500).

For SSNMR analysis, 3-week-old plants (before emergence of the inflorescence stem) were transferred to a glass fish tank with transparent fitted lid. The plants were further grown in an atmosphere enriched with ^{13}CO$_2$ (Sigma-Aldrich). About 0.4 to 0.7 g of ^{13}CO$_2$ gas was injected into the tank each morning before the light cycle started. The enclosure was cracked open by 10 cm during the dark cycle to reduce humidity. The inflorescence stems were collected when they reached 5 to 6 cm length (37–42 d) and were cut into 1-cm segments below the apical bud. Cauline leaves and siliques were removed, and stem segments were stored at −80°C. These cell wall samples were ~30% statistically labeled, estimated by comparing the intramolecular spin diffusion efficiencies of these stem cell walls with a uniformly labeled seedling sample (Wang et al., 2015).

Cell Wall Composition Analysis

Stem segments were ground in liquid nitrogen and incubated with shaking in 1.5% SDS at room temperature for 16 h to remove proteins and membranes and to inactivate endogenous wall enzymes. Cell wall residues were rinsed six times with distilled, deionized water and the wash with 1.5% SDS was repeated, then cell wall residues were washed 10 times with distilled, deionized water. Samples were treated overnight at 37°C with α-amylase from porcine pancreas (100 units mL^{-1}) to remove starch with NaN$_3$ (0.02%) to inhibit microbial growth. Cell walls were washed three times with distilled, deionized water, incubated with shaking in 1.5% SDS at room temperature for 10 h, and then washed 10 times with distilled, deionized water. This cell wall preparation was used for monosaccharide analysis, cellulose content determination, and SSNMR experiments. For SSNMR analysis, the never-dried Arabidopsis samples were centrifuged at room temperature at 1,000*g* for 5 min and 5,000*g* for 90 min to reach a hydration level of ~40 weight %.

The monosaccharide analysis protocol was adapted from the methods of De Ruiter et al. (1992) and Wang et al. (2013). In brief, 1 mg of dry cell wall powder and 500 μL of 3 N methanolic hydrochloric acid were mixed and incubated at 80°C for 16 h, cooled on ice, and dried with filtered air. Two hundred microliters of 2 M TFA was added to the dried residue, mixed thoroughly, incubated at 121°C for 2 h in a sealed tube, and cooled on ice. Samples were centrifuged at 14,000*g*, and supernatants (containing the hydrolyzed matrix) were removed and air dried. The insoluble residue, predominantly cellulose, was hydrolyzed with 500 μL of 72% H$_2$SO$_4$ at room temperature for 1 h. Samples were then diluted with distilled, deionized water to a concentration of 2 M H$_2$SO$_4$ and incubated at 100°C for 2 h with frequent vortexing, then neutralized with NH$_4$OH and air dried. All samples (both supernatant and residue) were resuspended with distilled, deionized water and filtered with 0.2-μm Millex-LG syringe-driven filter cartridges and analyzed by anion-exchange chromatography with pulsed amperometric detection on a CarboPac PA20 column at a flow rate of 0.5 mL min^{-1} (Dionex ICS-5000 Capillary Reagent-Free IC System). The loaded column was eluted with 10 mM sodium hydroxide for 15 min, then ramped to an equal mixture of 100 mM sodium hydroxide and 100 mM sodium acetate over 25 min. Sugar composition analysis (Tables I and II) was used to estimate the relative concentrations of pectin, XyG, xylan, and cellulose in segments #1 to #4 and the base of the stem. The data are based on one set of ~50 ground stems with three separate samples measured as above for each segment, with two technical replicates, for a total of six measurements for each segment.

To assess polysaccharide losses (solubilization) by our wall preparation procedure, we ground inflorescence segments in 20 mM MES buffer or 1% SDS, incubated overnight, precipitated the extract with ice-cold ethanol, and measured total sugar content of the precipitated material (Albalasmeh et al., 2013). Solubilized polysaccharide was ~5% of the total wall polysaccharide content and was the same for segments #1 to #4. This shows that inflorescence walls incurred negligible loss of wall structural material, and there was no evidence for differential losses along the growth gradient.

Lignin content was determined by measuring the fluorescence intensity after staining stem cross sections with basic fuchsin (Kapp et al., 2015). Stem segments were frozen in cryomatrix and sectioned with a cryomicrotome (Leica CM1950 cryostat). The 40-μm sections were incubated in 0.001% basic fuchsin for 5 min at 100 rpm, washed with distilled, deionized water for 10 min, washed twice with 50% glycerol for 10 min, and rinsed in distilled, deionized water. The sections were imaged with the Cy3 filter (565 nm wavelength) on an Olympus

BX63 (Chroma 49005 filter). The intensity of the section area was measured using Olympus cellSens software.

Mechanical Measurements

For stress/strain assays, stems from 5- to 6-cm-tall primary inflorescences were frozen at −80°C, thawed, cut in 1-cm segments matching the growth analysis, and flattened between glass slides under 700 g for 10 min. Segments were clamped in a custom-built extensometer with 3 mm between clamps and extended in two cycles to a maximum of 40 g of force (390 mN) at 3 mm min^{-1}. The slopes at the end of the two stress/strain curves were used to calculate the plastic and elastic compliances of the walls (Cosgrove, 2011) and are expressed as fractional change in length per N force. These compliances are comparable among samples if there is an equal amount of wall material per cross section, which we estimated by proxy as dry weight per 1-cm segment of the inflorescence stem: frozen/thawed/flattened segments were washed in 1.5% SDS for 24 h, rinsed in six changes of water, freeze dried, and weighed. The values (means ± SE in mg; $n = 5$) were as follows: #1, 0.62 ± 0.07; #2, 0.61 ± 0.05; #3, 0.62 ± 0.04; and #4, 0.61 ± 0.05. Student's t tests indicated no significant difference at $P < 0.05$. Without SDS washing, dry weights of the segments were nearly double these values, presumably due to relatively high cytoplasmic contents, but not statistically different from each other. SDS extracts showed negligible wall polysaccharide (see above), so the SDS-extracted weights are taken as better estimates of wall material per length.

SANS Measurements

SANS measurements were conducted at the Bio-SANS instrument at the High-Flux Isotope Reactor, Oak Ridge National Laboratory (Heller et al., 2014). The three different instrument configurations employed to cover the range, $0.003 < Q$ (Å^{-1}) < 0.7, of scattering vectors with sufficient overlap had sample-to-detector distances of 1.13, 6.83, and 15.33 m at a wavelength of 6 Å ($\Delta\lambda/\lambda$ = 0.15). The center of the moveable area detector (1 m × 1 m; GE-Reuter Stokes Tube Detector) was offset by 350 mm from the beam center to cover the required Q range. The scattering intensity profiles $I(Q)$ versus Q were obtained by azimuthally averaging the processed 2D images, which were normalized to incident beam monitor counts, and corrected for detector dark current, pixel sensitivity, and scattering from the titanium quartz cell. Plant stem segments, prepared as for mechanical analysis, were washed in 2% SDS for 12 h, flattened between slides with a 700-g weight, and washed in SDS for three additional cycles (48 h total), then equilibrated in water. Prior to SANS measurement, they were equilibrated in D_2O/water solvents (100 and 35% D_2O) for at least 24 h with several changes of solvent. The stems (10–12 stems, 1 cm in length) were vertically aligned in titanium cells, which were filled with equilibration solvent for SANS measurements.

SANS data analysis was carried out using the Irena evaluation routine implemented in commercially available Igor Pro software (Ilavsky and Jemian, 2009). A multilevel unified fit was used to describe the multiple levels of structural organization evident in the scattering data (Beaucage, 1995, 1996). In this method, the scattering provided by each structural level is the sum of a Guinier exponential form and a structurally limited power-law tail. A generalized equation representing any number of spherical levels is written as follows (Beaucage, 1995, 1996):

$$I(Q) = \sum_{\mathrm{i}=1}^{\mathrm{n}} \mathrm{G_i} \exp\left(\frac{-Q^2R_{\mathrm{gi}}^2}{3}\right) + \mathrm{B_i} \exp\left(\frac{-Q^2R_{\mathrm{g(i+1)}}^2}{3}\right)\left[\frac{(\mathrm{erf}(QR_{\mathrm{gi}}/\sqrt{6}))^3}{Q}\right]^{\mathrm{Pi}} \tag{1}$$

where n is the number of structural levels observed, G is the Guinier prefactor, R_g is the radius of gyration, and B is a prefactor specific to the type of power-law scattering, which is specified as the decay of the exponent P. Error analysis was performed using the least-squares fitting approach for nonlinear functions in order to properly account for correlated parameters, which is available as analyze uncertainty in the unified fit implementation of the Irena evaluation routine.

Additionally, the presence of a correlation peak was observed in the high-Q region of segments #1 and #4 measured in 100% D_2O and was attributed to the cellulose microfibrils. The degree of correlation distance between the correlated particles was analyzed using the unified fit approach, as described previously (Stribeck, 2007; Cardoso et al., 2010). The correlation effect is incorporated into the general scattering intensity description as follows (Beaucage et al., 1995):

$$I(Q) = \mathrm{A}\ \mathrm{F}(Q)^2\ \mathrm{S}(Q) \tag{2}$$

where $\mathrm{AF}(Q)^2$ is the scattered intensity for noncorrelated particles and corresponds to Equation 1 (Beaucage et al., 1995). S(Q) is the structure factor that, in the unified fit, accounts for weak correlations between the particles and was only applied to modify the high-Q structural level. All remaining structural levels were not affected by S(Q). In the unified fit method, a semiempirical function based on the Born-Green theory that describes the correlations between the particles is given by

$$\mathrm{S}(Q) = \frac{1}{1+\mathrm{k}\Theta} \tag{3}$$

and

$$\Theta = 3\,\frac{\sin(Q\zeta) - q\zeta\cos(Q\zeta)}{(Q\zeta)^3} \tag{4}$$

where k is the degree of correlation and ζ is the averaged distance between the correlated particles (Beaucage et al., 1995). The spherical particle correlation function implemented in the unified fit function of the Irena package was applied to the high-Q data to extract the correlation distance between neighboring cellulose fibrils.

SSNMR Spectroscopy

All SSNMR spectra of inflorescence cell walls were measured on an 800-MHz Bruker AVANCE II spectrometer at 18.8 T using a 3.2-mm MAS probe. Typical radiofrequency field strengths were 50 to 62.5 kHz for ^{13}C and 50 to 80 kHz for ^{1}H. All ^{13}C chemical shifts were externally referenced to the adamantine CH_2 peak at 38.48 ppm on the tetramethylsilane scale.

1D ^{13}C MAS spectra were measured at 298 K using ^{1}H-^{13}C CP or ^{13}C DP to create the initial ^{13}C transverse magnetization. Quantitative ^{13}C DP spectra were measured using a long recycle delay of 30 s to detect all polysaccharide signals. CP spectra preferentially detect rigid molecules such as cellulose, while DP spectra with a short recycle delay of 2 s preferentially detect the mobile polysaccharide signals. ^{13}C DP and ^{13}C CP spectra were measured under 10 kHz MAS at 293 K. A spin-lock contact time of 0.5 ms and a recycle delay of 2 s were used for CP spectra. Refocused INEPT (Elena et al., 2005) spectra were measured under 13.5 kHz MAS at 293 K to selectively detect highly dynamic segments such as pectin side chains. A recycle delay of 3.5 s and a total polarization transfer time of 6 ms, which consists of two delays of 1.8 ms followed by two delays of 1.2 ms, were used for the INEPT experiments. These delays correspond to $1/(4\mathrm{J_{CH}})$ and $1/(6\mathrm{J_{CH}})$, respectively, assuming a standard $^{1}\mathrm{J_{CH}}$ value of 140 Hz. The experimental times range from 0.5 to 4 h for 512 scans depending on the recycle delay.

2D refocused J-INADEQUATE experiments (Cadars et al., 2007) correlating double-quantum and single-quantum ^{13}C chemical shifts were conducted at 298 K under 12 kHz MAS to resolve and assign the ^{13}C chemical shifts. To preferentially detect mobile components of the cell wall, ^{13}C DP with a recycle delay of 2 s was used to excite the initial ^{13}C magnetization. A total of 320 t_1 increments were collected, and the number of scans per t_1 increment was 128 for segment #1 and 96 for segment #4, resulting in experiment times of 23 and 17 h, respectively.

CP-based 2D ^{1}H-driven spin diffusion spectra were measured to resolve and assign multiple forms of cellulose microfibrils (Wang et al., 2016c). The mixing times were 100 ms for inflorescence samples and 30 ms for the seedling cell wall to compensate for the partial (~30%) labeling of inflorescence cell walls. ^{1}H-driven spin diffusion spectra of inflorescence cell walls with spin diffusion time of 100 ms were measured under 11 kHz at 298 K with a recycle delay of 1.9 s. A total of 450 t_1 increments were collected, and the number of scans per t_1 increment was 128 for segment #1 and 160 for segment #4, for total experiment times of 32 and 40 h, respectively.

2D dipolar-edited ^{1}H-^{13}C MELODI-HETCOR experiments (Yao and Hong, 2001; Yao et al., 2001) were conducted at 298 K under 14.8 kHz MAS to measure the water-polysaccharide correlations. ^{1}H chemical shifts were calibrated using formyl-Met-Leu-Phe-OH (Li et al., 2010). ^{1}H homonuclear decoupling was achieved using the FSLG sequence (Bielecki et al., 1989) with a transverse ^{1}H field strength of 80 kHz. Before ^{1}H t_1 evolution, eight rotor periods of C-H dipolar dephasing were used to destroy the ^{1}H magnetization of ^{13}C-labeled polysaccharides and retain only the water ^{1}H signals. A 1-ms ^{1}H-^{1}H spin diffusion was used. The usage of ^{1}H-^{13}C CP for polarization transfer suppresses highly mobile signals. A recycle delay of 1.8 s was used, and the experiment took about 15 h for segment #1, acquiring a total of 208 t_1 increments and 144 scans for each increment.

^{13}C-^1H DIPSHIFT experiments were carried out at 298 K under 7 kHz MAS to measure motional amplitudes (Munowitz et al., 1981). ^1H homonuclear decoupling was achieved using FSLG with a ^1H transverse field strength of 80 kHz. The scaling factor was verified using the model peptide formyl-Met-Leu-Phe-OH (Rienstra et al., 2002) to be 0.577. The ratio between the measured coupling and the FSLG-scaled rigid-limit coupling of 13.1 kHz gives the order parameters S_{CH} and S_{CH2} of C-H groups. To compare microsecond time scale dynamics, ^{13}C-detected ^1H $T_{1\rho}$ relaxation times were measured using a Lee-Goldburg spin-lock sequence in which ^1H spin diffusion was suppressed during the CP period (Cady and Hong, 2009). The effective ^1H spin-lock field was 62.5 kHz. Most relaxation curves were fit to a double-exponential function (Supplemental Table S1). A total of 15 t_1 increments were measured. Both CP-DIPSHIFT and quantitative DP-DIPSHIFT with recycle delays of 2 and 20 s, respectively, were used to detect the motional amplitude of the cellulose-contacting polysaccharide and the overall motional amplitude of all polysaccharides in the whole cell wall, respectively. Quantitative experiments took about 21 h, and CP-based experiments took about 2 h for 256 scans in segment #1 spectra.

Supplemental Data

The following supplemental materials are available.

Supplemental Figure S1. Cross sections of an Arabidopsis inflorescence stem at four positions along the axis, and fluorescence intensity divided by stem cross-sectional area.

Supplemental Figure S2. Examples of characteristic stress/strain curves for the Arabidopsis stem segments.

Supplemental Figure S3. Difference spectrum between the quantitative ^{13}C DP spectra of inflorescence and inflorescence cell walls.

Supplemental Figure S4. ^{13}C DP J-INADEQUATE spectra of inflorescence #1 and #4 cell walls with selected 1D cross sections.

Supplemental Figure S5. ^{13}C-^1H DIPSHIFT curves of inflorescence and seedling cell walls at 298 K.

Supplemental Figure S6. Microsecond time-scale motions of polysaccharides from ^1H $T_{1\rho}$ relaxation.

Supplemental Table S1. ^1H $T_{1\rho}$ relaxation times of inflorescence cell wall #1.

Supplemental Table S2. List of abbreviations used in the text.

ACKNOWLEDGMENTS

We thank Daniel Durachko, Edward Wagner, and Liza Wilson for technical assistance.

Received September 6, 2017; accepted October 29, 2017; published October 30, 2017.

LITERATURE CITED

Albalasmeh AA, Berhe AA, Ghezzehei TA (2013) A new method for rapid determination of carbohydrate and total carbon concentrations using UV spectrophotometry. Carbohydr Polym **97:** 253–261

Band LR, Úbeda-Tomás S, Dyson RJ, Middleton AM, Hodgman TC, Owen MR, Jensen OE, Bennett MJ, King JR (2012) Growth-induced hormone dilution can explain the dynamics of plant root cell elongation. Proc Natl Acad Sci USA **109:** 7577–7582

Bastien R, Legland D, Martin M, Fregosi L, Peaucelle A, Douady S, Moulia B, Höfte H (2016) KymoRod: a method for automated kinematic analysis of rod-shaped plant organs. Plant J **88:** 468–475

Beaucage G (1995) Approximations leading to a unified exponential/power-law approach to small-angle scattering. J Appl Cryst **28:** 717–728

Beaucage G (1996) Small-angle scattering from polymeric mass fractals of arbitrary mass-fractal dimension. J Appl Cryst **29:** 134–146

Beaucage G, Ulibarri TA, Black EP, Schaefer DW (1995) Multiple size scale structures in silica-siloxane composites studied by small-angle scattering. *In* JE Mark, CY Lee, PA Bianconi, eds, Hybrid Organic-Inorganic Composites, ACS Symposium Series, Vol 585. American Chemical Society, Washington DC, pp 97–111

Beusmans JMH, Silk WK (1988) Mechanical properties within the growth zone of corn roots investigated by bending experiments II. Distributions of modulus and compliance in bending. Am J Bot **75:** 996–1002

Bielecki A, Kolbert AC, Levitt MH (1989) Frequency-switched pulse sequences: homonuclear decoupling and dilute spin NMR in solids. Chem Phys Lett **155:** 341–346

Cadars S, Sein J, Duma L, Lesage A, Pham TN, Baltisberger JH, Brown SP, Emsley L (2007) The refocused INADEQUATE MAS NMR experiment in multiple spin-systems: interpreting observed correlation peaks and optimising lineshapes. J Magn Reson **188:** 24–34

Cady SD, Hong M (2009) Effects of amantadine on the dynamics of membrane-bound influenza A M2 transmembrane peptide studied by NMR relaxation. J Biomol NMR **45:** 185–196

Cardoso MB, Luckarift HR, Urban VS, O'Neill H, Johnson GR (2010) Protein localization in silica nanospheres derived via biomimetic mineralization. Adv Funct Mater **20:** 3031–3038

Chanliaud E, Gidley MJ (1999) In vitro synthesis and properties of pectin/*Acetobacter xylinus* cellulose composites. Plant J **20:** 25–35

Cosgrove DJ (2011) Measuring in vitro extensibility of growing plant cell walls. Methods Mol Biol **715:** 291–303

Cosgrove DJ (2014) Re-constructing our models of cellulose and primary cell wall assembly. Curr Opin Plant Biol **22:** 122–131

Cosgrove DJ (2016) Plant cell wall extensibility: connecting plant cell growth with cell wall structure, mechanics, and the action of wall-modifying enzymes. J Exp Bot **67:** 463–476

Cosgrove DJ, Cleland RE (1983) Osmotic properties of pea internodes in relation to growth and auxin action. Plant Physiol **72:** 332–338

Cosgrove DJ, Li ZC (1993) Role of expansin in cell enlargement of oat coleoptiles: analysis of developmental gradients and photocontrol. Plant Physiol **103:** 1321–1328

de O Buanafina MM (2009) Feruloylation in grasses: current and future perspectives. Mol Plant **2:** 861–872

De Ruiter GA, Schols HA, Voragen AG, Rombouts FM (1992) Carbohydrate analysis of water-soluble uronic acid-containing polysaccharides with high-performance anion-exchange chromatography using methanolysis combined with TFA hydrolysis is superior to four other methods. Anal Biochem **207:** 176–185

Dick-Pérez M, Zhang Y, Hayes J, Salazar A, Zabotina OA, Hong M (2011) Structure and interactions of plant cell-wall polysaccharides by two- and three-dimensional magic-angle-spinning solid-state NMR. Biochemistry **50:** 989–1000

Edelmann HG (1995) Water potential modulates extensibility of rye coleoptile cell-walls. Bot Acta **108:** 374–380

Elena B, Lesage A, Steuernagel S, Böckmann A, Emsley L (2005) Proton to carbon-13 INEPT in solid-state NMR spectroscopy. J Am Chem Soc **127:** 17296–17302

Erickson RO, Sax KB (1956) Elemental growth-rate of the primary root of *Zea mays*. Proc Am Philos Soc **100:** 487–498

Evered C, Majevadia B, Thompson DS (2007) Cell wall water content has a direct effect on extensibility in growing hypocotyls of sunflower (*Helianthus annuus* L.). J Exp Bot **58:** 3361–3371

Fenwick KM, Jarvis MC, Apperley DC (1997) Estimation of polymer rigidity in cell walls of growing and nongrowing celery collenchyma by solid-state nuclear magnetic resonance in vivo. Plant Physiol **115:** 587–592

Goldberg R (1984) Changes in the properties of cell-wall pectin methylesterase along the *Vigna radiata* hypocotyl. Physiol Plant **61:** 58–63

Goldberg R, Morvan C, Roland JC (1986) Composition, properties and localization of pectins in young and mature cells of the mung bean hypocotyl. Plant Cell Physiol **27:** 417–429

Goldberg R, Prat R (1982) Involvement of cell-wall characteristics in growth-processes along the mung bean hypocotyl. Plant Cell Physiol **23:** 1145–1154

Green PB (1976) Growth and cell pattern formation on an axis: critique of concepts, terminology, and modes of study. Bot Gaz **137:** 187–202

Hall H, Ellis B (2012) Developmentally equivalent tissue sampling based on growth kinematic profiling of Arabidopsis inflorescence stems. New Phytol **194:** 287–296

Heller WT, Urban VS, Lynn GW, Weiss KL, O'Neill HM, Pingali SV, Qian S, Littrell KC, Melnichenko YB, Buchanan MV, et al (2014) The

Bio-SANS instrument at the High Flux Isotope Reactor of Oak Ridge National Laboratory. J Appl Cryst **47:** 1238–1246

Ilavsky J, Jemian PR (2009) Irena: tool suite for modeling and analysis of small-angle scattering. J Appl Cryst **42:** 347–353

Kapp N, Barnes WJ, Richard TL, Anderson CT (2015) Imaging with the fluorogenic dye Basic Fuchsin reveals subcellular patterning and ecotype variation of lignification in *Brachypodium distachyon*. J Exp Bot **66:** 4295–4304

Levesque-Tremblay G, Pelloux J, Braybrook SA, Müller K (2015) Tuning of pectin methylesterification: consequences for cell wall biomechanics and development. Planta **242:** 791–811

Li S, Su Y, Luo W, Hong M (2010) Water-protein interactions of an arginine-rich membrane peptide in lipid bilayers investigated by solid-state nuclear magnetic resonance spectroscopy. J Phys Chem B **114:** 4063–4069

Lin D, Lopez-Sanchez P, Gidley MJ (2015) Binding of arabinan or galactan during cellulose synthesis is extensive and reversible. Carbohydr Polym **126:** 108–121

Martínez-Sanz M, Gidley MJ, Gilbert EP (2016) Hierarchical architecture of bacterial cellulose and composite plant cell wall polysaccharide hydrogels using small angle neutron scattering. Soft Matter **12:** 1534–1549

McQueen-Mason S, Durachko DM, Cosgrove DJ (1992) Two endogenous proteins that induce cell wall extension in plants. Plant Cell **4:** 1425–1433

Munowitz MG, Griffin RG, Bodenhausen G, Huang TH (1981) Two-dimensional rotational spin-echo nuclear magnetic-resonance in solids: correlation of chemical-shift and dipolar interactions. J Am Chem Soc **103:** 2529–2533

Park YB, Lee CM, Kafle K, Park S, Cosgrove DJ, Kim SH (2014) Effects of plant cell wall matrix polysaccharides on bacterial cellulose structure studied with vibrational sum frequency generation spectroscopy and x-ray diffraction. Biomacromolecules **15:** 2718–2724

Peaucelle A, Braybrook S, Höfte H (2012) Cell wall mechanics and growth control in plants: the role of pectins revisited. Front Plant Sci **3:** 121

Refrégier G, Pelletier S, Jaillard D, Höfte H (2004) Interaction between wall deposition and cell elongation in dark-grown hypocotyl cells in Arabidopsis. Plant Physiol **135:** 959–968

Rienstra CM, Tucker-Kellogg L, Jaroniec CP, Hohwy M, Reif B, McMahon MT, Tidor B, Lozano-Pérez T, Griffin RG (2002) De novo determination of peptide structure with solid-state magic-angle spinning NMR spectroscopy. Proc Natl Acad Sci USA **99:** 10260–10265

Sánchez-Bravo J, Ortuño AM, Botía JM, Acosta M, Sabater F (1992) The decrease in auxin polar transport down the lupin hypocotyl could produce the indole-3-acetic acid distribution responsible for the elongation growth pattern. Plant Physiol **100:** 108–114

Silk WK (1984) Quantitative descriptions of development. Annu Rev Plant Physiol **35:** 479–518

Silk WK, Bogeat-Triboulot MB (2014) Deposition rates in growing tissue: implications for physiology, molecular biology, and response to environmental variation. Plant Soil **374:** 1–17

Spollen WG, Sharp RE (1991) Spatial distribution of turgor and root growth at low water potentials. Plant Physiol **96:** 438–443

Stribeck N (2007) X-Ray Scattering of Soft Matter. Springer, Berlin

Suh MC, Samuels AL, Jetter R, Kunst L, Pollard M, Ohlrogge J, Beisson F (2005) Cuticular lipid composition, surface structure, and gene expression in Arabidopsis stem epidermis. Plant Physiol **139:** 1649–1665

Wang T, Chen Y, Tabuchi A, Cosgrove DJ, Hong M (2016a) The target of β-expansin EXPB1 in maize cell walls from binding and solid-state NMR studies. Plant Physiol **172:** 2107–2119

Wang T, Park YB, Caporini MA, Rosay M, Zhong L, Cosgrove DJ, Hong M (2013) Sensitivity-enhanced solid-state NMR detection of expansin's target in plant cell walls. Proc Natl Acad Sci USA **110:** 16444–16449

Wang T, Park YB, Cosgrove DJ, Hong M (2015) Cellulose-pectin spatial contacts are inherent to never-dried Arabidopsis primary cell walls: evidence from solid-state nuclear magnetic resonance. Plant Physiol **168:** 871–884

Wang T, Phyo P, Hong M (2016b) Multidimensional solid-state NMR spectroscopy of plant cell walls. Solid State Nucl Magn Reson **78:** 56–63

Wang T, Salazar A, Zabotina OA, Hong M (2014) Structure and dynamics of *Brachypodium* primary cell wall polysaccharides from two-dimensional ^{13}C solid-state nuclear magnetic resonance spectroscopy. Biochemistry **53:** 2840–2854

Wang T, Yang H, Kubicki JD, Hong M (2016c) Cellulose structural polymorphism in plant primary cell walls investigated by high-field 2D solid-state NMR spectroscopy and density functional theory calculations. Biomacromolecules **17:** 2210–2222

Wang T, Zabotina O, Hong M (2012) Pectin-cellulose interactions in the Arabidopsis primary cell wall from two-dimensional magic-angle-spinning solid-state nuclear magnetic resonance. Biochemistry **51:** 9846–9856

Went FW, Thimann KV (1937) Phytohormones. MacMillan, New York

White PB, Wang T, Park YB, Cosgrove DJ, Hong M (2014) Water-polysaccharide interactions in the primary cell wall of *Arabidopsis thaliana* from polarization transfer solid-state NMR. J Am Chem Soc **136:** 10399–10409

Xiao C, Somerville C, Anderson CT (2014) POLYGALACTURONASE INVOLVED IN EXPANSION1 functions in cell elongation and flower development in *Arabidopsis*. Plant Cell **26:** 1018–1035

Yao XL, Hong M (2001) Dipolar filtered ^{1}H-^{13}C heteronuclear correlation spectroscopy for resonance assignment of proteins. J Biomol NMR **20:** 263–274

Yao XL, Schmidt-Rohr K, Hong M (2001) Medium- and long-distance ^{1}H-^{13}C heteronuclear correlation NMR in solids. J Magn Reson **149:** 139–143

Zhang T, Vavylonis D, Durachko DM, Cosgrove DJ (2017) Nanoscale movements of cellulose microfibrils in primary cell walls. Nat Plants **3:** 17056

Zhang T, Zheng Y, Cosgrove DJ (2016) Spatial organization of cellulose microfibrils and matrix polysaccharides in primary plant cell walls as imaged by multichannel atomic force microscopy. Plant J **85:** 179–192

Zhao Q, Yuan S, Wang X, Zhang Y, Zhu H, Lu C (2008) Restoration of mature etiolated cucumber hypocotyl cell wall susceptibility to expansin by pretreatment with fungal pectinases and EGTA in vitro. Plant Physiol **147:** 1874–1885

Zykwinska A, Gaillard C, Buléon A, Pontoire B, Garnier C, Thibault JF, Ralet MC (2007a) Assessment of in vitro binding of isolated pectic domains to cellulose by adsorption isotherms, electron microscopy, and x-ray diffraction methods. Biomacromolecules **8:** 223–232

Zykwinska A, Thibault JF, Ralet MC (2007b) Organization of pectic arabinan and galactan side chains in association with cellulose microfibrils in primary cell walls and related models envisaged. J Exp Bot **58:** 1795–1802

Zykwinska A, Thibault JF, Ralet MC (2008) Competitive binding of pectin and xyloglucan with primary cell wall cellulose. Carbohydr Polym **74:** 957–961

Zykwinska AW, Ralet MC, Garnier CD, Thibault JF (2005) Evidence for in vitro binding of pectin side chains to cellulose. Plant Physiol **139:** 397–407